3D Mesoporous van der Waals Heterostructures for Trifunctional Energy Electrocatalysis

Cheng Tang, Ling Zhong, Bingsen Zhang, Hao-Fan Wang, and Qiang Zhang*

The emergence of van der Waals (vdW) heterostructures of 2D materials has opened new avenues for fundamental scientific research and technological applications. However, the current concepts and strategies of material engineering lack feasibilities to comprehensively regulate the as-obtained extrinsic physicochemical characters together with intrinsic properties and activities for optimal performances. A 3D mesoporous vdW heterostructure of graphene and nitrogen-doped MoS_2 via a two-step sequential chemical vapor deposition method is constructed. Such strategy is demonstrated to offer an all-round engineering of 2D materials including the morphology, edge, defect, interface, and electronic structure, thereby leading to robustly modified properties and greatly enhanced electrochemical activities. The hydrogen evolution is substantially accelerated on MoS_2, while the oxygen reduction and evolution are significantly improved on graphene. This work provides a powerful overall engineering strategy of 2D materials for electrocatalysis, which is also enlightening for other nanomaterials and energy-related applications.

Since the first isolation of graphene in 2004,[1] the flourish of 2D materials not only provides versatile platforms for fundamental scientific research, but also opens new avenues for technological applications, which is attributed to their unique structure and impressive properties. Particularly, massive efforts have been devoted to explore the possibilities of 2D materials (graphene, transition-metal dichalcogenide (TMD), layered double hydroxides (LDHs), etc.) in energy electrocatalysis in the last couple of years, including hydrogen evolution reaction (HER),[2] oxygen reduction reaction (ORR),[3] and oxygen evolution reaction (OER),[4,5] aiming at cost-efficient and highly effective technologies for the future energy scenario. Furthermore, the emergence of van der Waals (vdW) heterostructures invokes new feasibilities to achieve full potential of 2D materials by combining components with different properties and functionalities.[6–10] Up to date, various vdW heterostructures have been demonstrated to exhibit significantly improved electrocatalytic activities, such as graphene/TMD for HER,[7,11–13] graphene/NiFe LDHs for OER,[14,15] Ti_3C_2/g-C_3N_4 for ORR/OER,[16] etc.

It is notable that for the gas-involved heterogeneous electrocatalysis, both the intrinsic electrocatalytic activity and extrinsic physicochemical characters are crucial for the apparent activities.[17] The vdW-bonded hybridization is able to compensate the individual weakness,[8] endow charge transfer between layers,[10] and decrease the interfacial contact resistance,[14,18] thereby leading to enhanced inherent activities.[7,9,14,18] Nevertheless, these vdW heterostructures are mainly constructed through layer-by-layer assembly in liquid or direct growth by chemical vapor deposition (CVD) on lamellar substrates, which lack capability to regulate the as-obtained physicochemical characters, such as the hierarchical porosity and nanostructures. Therefore, smart design and versatile techniques are urgently required for the controllable construction of advanced vdW heterostructures, aiming at a comprehensive optimization of both intrinsic electrocatalytic activity and extrinsic physicochemical characters for enhanced performances.
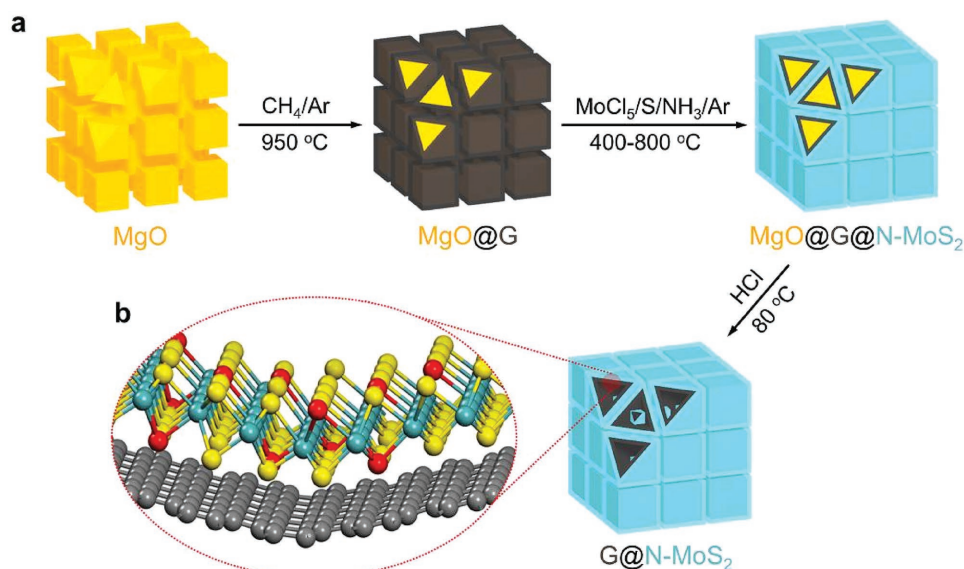
In this contribution, we designed a 3D mesoporous graphene/nitrogen-doped MoS_2 vdW heterostructure (G@N-MoS_2) and devised a two-step sequential CVD method to facilely synthesize such vdW solid materials (**Figure 1**a). A mesoporous graphene framework was grown via templated CVD in advance, and then nanosized N-MoS_2 was uniformly deposited over it with the formation of a vertical vdW heterostructure (Figure 1b). The as-proposed strategy is demonstrated to effectively modify the physical and electronic structure of both components, and the integrated morphology and interfacial coupling as well. Consequently, the construction of G@N-MoS_2 offers a versatile platform for the all-round engineering of nanomaterials toward significantly enhanced electrocatalytic performances. It is revealed that the HER activity is significantly enhanced on the N-MoS_2 side with a low overpotential of 243 mV for 10 mA cm^{-2}, while the ORR and OER activities are substantially improved on the graphene side with a potential gap around 0.90 V, suggesting promising activities for trifunctional electrocatalysis. The material design and synthetic strategy are believed to afford emerging opportunities and inspiration for the research of 2D materials and energy electrocatalysis.

C. Tang, L. Zhong, H.-F. Wang, Prof. Q. Zhang
Beijing Key Laboratory of Green Chemical Reaction Engineering and Technology
Department of Chemical Engineering
Tsinghua University
Beijing 100084, P. R. China
E-mail: zhang-qiang@mails.tsinghua.edu.cn
Prof. B. Zhang
Shenyang National Laboratory for Material Science
Institute of Metal Research
Chinese Academy of Sciences
Shenyang 110016, P. R. China

The ORCID identification number(s) for the author(s) of this article can be found under https://doi.org/10.1002/adma.201705110.

**ADVANCED
SCIENCE NEWS**
www.advancedsciencenews.com

**ADVANCED
MATERIALS**
www.advmat.de

Figure 1. Schematic illustration of the synthesis of 3D mesoporous G@N-MoS$_2$ heterostructures. a) The two-step sequential CVD method, including CVD growth of mesoporous graphene on porous MgO templates at a high temperature, and then the in situ deposition of N-MoS$_2$ at a low temperature. b) Schematic representation of G@N-MoS$_2$ exhibiting the vdW heterostructure with nitrogen doping and topological curvature. C atoms are indicated in gray, while Mo atoms in green, S atoms in yellow, and N atoms in red.

The 3D mesoporous G@N-MoS$_2$ heterostructure was fabricated under the synthetic procedure as illustrated in Figure 1. First, Mg(OH)$_2$-derived MgO was synthesized and adopted as mesoporous template for the two-step sequential CVD growth of graphene and N-MoS$_2$. Then, a thin layer of graphene was deposited on MgO using CH$_4$ as carbon source at 950 °C,[19] followed by the in situ deposition of N-MoS$_2$ using MoCl$_5$, sulfur, and NH$_3$ as precursor materials at 800 °C.[20] Finally, the 3D mesoporous G@N-MoS$_2$ can be achieved after the removal of MgO templates with HCl etching. Other counterparts, such as undoped hybrid (G@MoS$_2$) and individual components (G, MoS$_2$, N-MoS$_2$) were also fabricated to probe the growth behavior and activity mechanism (see details in Supporting Information).

Scanning electron microscopy (SEM) combined with high-angle annular dark field-scanning transmission electron microscopy (HAADF-STEM) images reveal that the as-synthesized G@N-MoS$_2$ exhibits a hexagonal appearance replicated from MgO (**Figure 2**a), with a mesoporous graphene framework as the scaffold and nanosized N-MoS$_2$ uniformly distributed over it (Figure 2b, Figure S1, Supporting Information). Notably, the as-deposited graphene on MgO (sample G) is dominantly monolayer or bilayer with a specific surface area as high as 2211 m^2 g^{-1} (Figure S2, Supporting Information) and regularly constructs into a mesoporous framework with interconnected mesopores (Figure S3, Supporting Information). After the growth of N-MoS$_2$, the mesoporous structure is retained; however, the wall of the mesopores is obviously thicker, indicating the addition of a thin layer of N-MoS$_2$ on the surface of graphene and thereby the formation of G@N-MoS$_2$ vdW heterostructure (Figure 2c, Figure S3a, Supporting Information). The high-resolution transmission electron microscopy (HRTEM) image clearly proves the presence of N-MoS$_2$ with an interlayer distance of 0.62 nm, which is curved along

the mesoporous wall (Figure 2d) and tiled on the underneath graphene (Figure 2e), forming a layer-by-layer stacking. The N-MoS$_2$ nanosheets dominantly exhibit a lateral size smaller than 20 nm and a thin thickness within three layers (Figure S4, Supporting Information). Due to the remarkable resemblance of the ultrathin 2D layered structure, it is technically difficult to distinguish graphene from N-MoS$_2$ in such 3D mesoporous scaffold as shown in Figure 2d. Fortunately, assisted by a thicker graphene sheet in few cases, the interface between graphene and N-MoS$_2$ can be clearly observed, which no doubt confirms the characteristic layer-by-layer stacking (with different interlayer distance) in vdW heterostructures (Figure 2f, Figure S5, Supporting Information). The fast Fourier transform of the HRTEM image delivers two sets of diffraction spots assigned to (103) and (006) crystal planes of 2H MoS$_2$ (JCPDF No. 77–1716), respectively (Figure S6, Supporting Information). The imperfection in typical hexagonal diffraction spots is ascribed to the 3D mesoporous structure with abundant topological and basal defects (Figure 2g). The electron energy loss spectroscopy (EELS) confirms the existence of C, Mo, S, and N (Figure S7, Supporting Information). All these elements are uniformly distributed in the 3D mesoporous framework, indicating a homogeneous incorporation of N into MoS$_2$ planes and uniform dispersion of N-MoS$_2$ on graphene (Figure 2h).

The G@N-MoS$_2$ vdW heterostructure was further investigated by X-ray diffraction (XRD) patterns, X-ray photoelectron spectroscopy (XPS), and Raman spectroscopy. All diffraction peaks in the XRD patterns (**Figure 3**a) and the high-resolution Mo 3d /S 2p XPS spectra (Figurse S8 and S9, Supporting Information) for G@N-MoS$_2$ are consistent with hexagonal 2H MoS$_2$ crystal,[7,21,22] indicating that the hybridization with graphene and incorporation of nitrogen do not influence the crystal structure. The characteristic Raman peaks centered at 1360 and 1560 cm^{-1} recorded using 633 nm line are assigned to the

**ADVANCED
SCIENCE NEWS**

www.advancedsciencenews.com

**ADVANCED
MATERIALS**

www.advmat.de
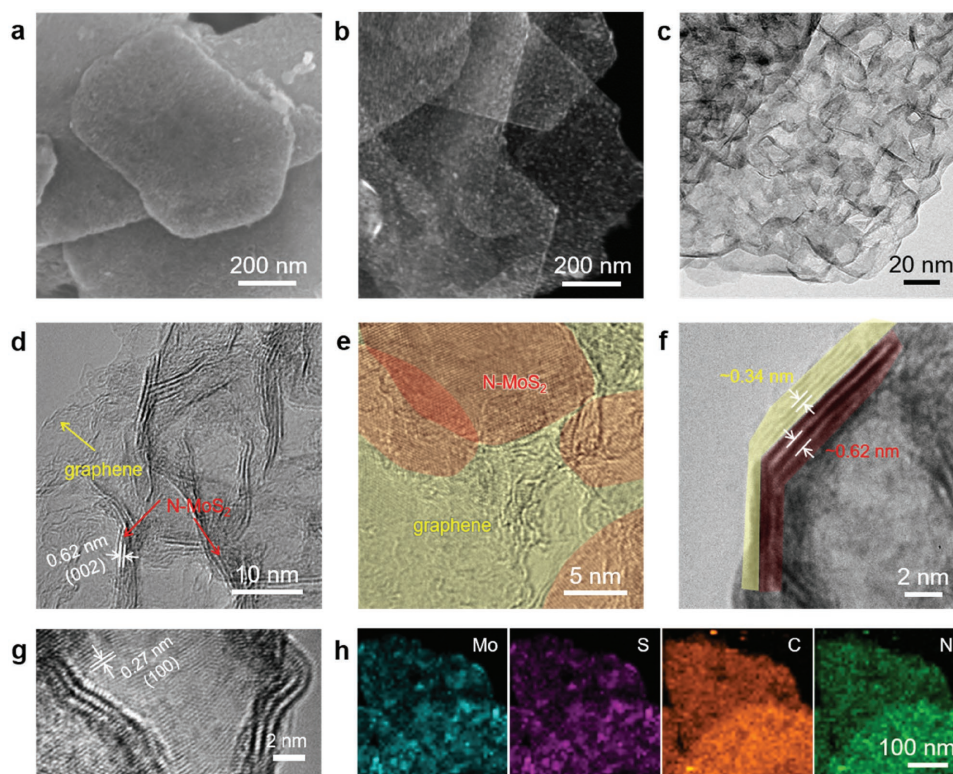
Figure 2. Morphological and structural characterizations of 3D mesoporous G@N-MoS$_2$ heterostructures. a) SEM image, b) HAADF-STEM image, and c–g) HRTEM images of G@N-MoS$_2$. Panels (e) and (f) confirm the vdW heterostructure of graphene (pseudocolored in yellow) and N-MoS$_2$ (pseudocolored in red) from two modes, which are schematically shown in Figure S5 (Supporting Information) with the primary images. Panel (g) shows the edges and defects in N-MoS$_2$. h) Elemental mappings of G@N-MoS$_2$ for C, Mo, S, and N.

so-called D and G peaks for graphene (Figure S10, Supporting Information), and the peaks around 382, 404 cm^{-1} recorded using 532 nm line correspond to the in-plane E^1_{2g} and out-of-plane A_{1g} vibration modes of 2H MoS$_2$ phase, respectively (Figure 3b).[23,24] The obviously smaller frequency difference ($\Delta = 22.3$ cm^{-1}) value for G@N-MoS$_2$ indicates the decrease of MoS$_2$ thickness (corresponding to bilayer)[24,25] compared with G@MoS$_2$, in consistence with the HRTEM images (Figure 2d, Figures S4 and S11, Supporting Information). Besides, the intensity ratio of A_{1g}/E^1_{2g} is increased for G@N-MoS$_2$, which

can be attributed to the stretching vibrational modes of additional Mo−N bonds around 404 cm^{-1}.[23] The successful incorporation of N atoms into the MoS$_2$ matrix by substituting the basal S atoms is further supported by the obvious hump generated at 398 eV in the Mo 3p XPS spectrum.[23,26]

Based on above results, a 3D mesoporous vdW heterostructure of graphene and N-MoS$_2$ was successfully synthesized with a thin layer thickness, hierarchical porosity, tunable electronic structures, and exquisite hybridization of 2D materials. It is attributed to the proposed two-step sequential CVD method
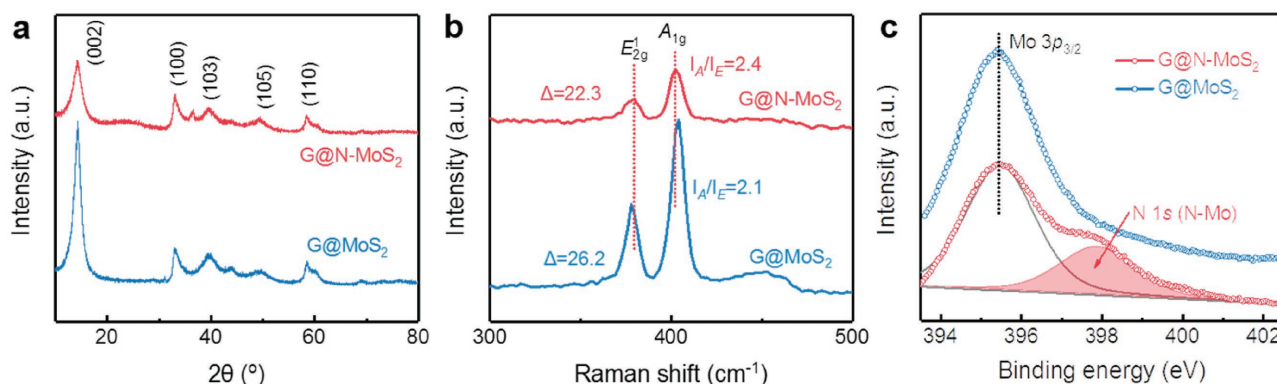
Figure 3. Chemical composition of 3D mesoporous G@(N-)MoS$_2$ heterostructures. a) XRD patterns of G@N-MoS$_2$ in comparison with G@MoS$_2$. b) Raman spectra obtained using 532 nm lines. c) XPS spectra covering N 1s and Mo 3p$_{3/2}$ orbitals.

**ADVANCED
SCIENCE NEWS**
www.advancedsciencenews.com

**ADVANCED
MATERIALS**
www.advmat.de

on mesoporous MgO templates. First, the MgO not only serves as a favorable 3D template for the morphology replication, but also exhibits beneficial catalytic activity to manipulate the growth of graphene and N-MoS$_2$.[19] Second, the mesoporous MgO@G scaffolds spatially confine the subsequent growth of nanosized N-MoS$_2$ with local curvatures. Besides, the previous deposition of graphene on MgO is critical to modify the interaction between N-MoS$_2$ and substrate, therefore providing a more desirable surface for the self-limiting precipitation of N-MoS$_2$ species.[20] Furthermore, the introduction of NH$_3$ gas during the deposition of N-MoS$_2$ is supposed to reduce the partial pressure of gaseous N-MoS$_2$ species and give rise to a thinner N-MoS$_2$ nanosheets.[20] Eventually, the as-obtained heterostructure exhibits 3D interconnected pathway, intimate interfacial interaction, enriched edge sites, and abundant in-plane defects, which is beneficial for gas-involved heterogeneous electrocatalysis.

To investigate the impact of as-demonstrated all-round engineering strategy and 3D mesoporous vdW heterostructure on electrocatalytic activities, we first studied the HER performance for G@N-MoS$_2$ and other control samples. **Figure 4**a presents the linear sweep voltammetry (LSV) polarization curves for HER obtained in N$_2$-saturated 0.50 M H$_2$SO$_4$ with a catalyst loading of ≈0.25 mg cm^{-2}. It reveals that the hybridization with graphene can substantially improve the activity of (N-)MoS$_2$, with the overpotential required for a current density of 10 mA cm^{-2} (η_{10}) reduced by 302 mV for MoS$_2$ and 87 mV for N-MoS$_2$. Besides, the nitrogen doping in MoS$_2$ is demonstrated

to further increase the HER activity, with decreased η_{10} by 260 mV for MoS$_2$ and 45 mV for G@MoS$_2$. As a result, the G@N-MoS$_2$ catalyst exhibits the best HER activity with a low η_{10} of 243 mV, which is comparable with previously reported MoS$_2$ catalysts[25,27] and some vdW heterostructures.[12,13,28]

Furthermore, the Tafel slopes derived at low overpotentials were used to analyze the HER kinetics (Figure 4b). Although the Tafel slope can be decreased after the sole graphene hybridization (G@MoS$_2$) or nitrogen incorporation (N-MoS$_2$), the values are yet close to 120 mV dec^{-1}, indicating that the rate-limiting step is still the Volmer reaction (hydrogen adsorption, 120 mV dec^{-1}). For G@N-MoS$_2$, however, the Tafel slope is significantly decreased to 82.5 mV dec^{-1}, which falls between the Volmer mechanism (120 mV dec^{-1}) and Heyrovsky mechanism (electrochemical desorption, 40 mV dec^{-1}). The hydrogen binding on N-MoS$_2$ is supposed to be modified by the strong interaction between the mesoporous graphene substrate and N-MoS$_2$,[29] leading to favorable adsorption energies and accelerated HER kinetics. Moreover, the G@N-MoS$_2$ exhibits excellent long-term durability, with a nearly overlapped LSV curves after 1000 cyclic voltammetry (CV) cycles (Figure 4c), suggesting the G@N-MoS$_2$ heterostructure as a promising candidate for HER electrocatalysis (Table S1, Supporting Information).

Electrochemical impedance spectroscopy (EIS) and electrochemical active surface area (ECSA) were further measured to investigate the electrode kinetics and elucidate the performance enhancement. After the hybridization with conductive graphene framework, the charge-transfer resistance (R_{ct}) for G@MoS$_2$
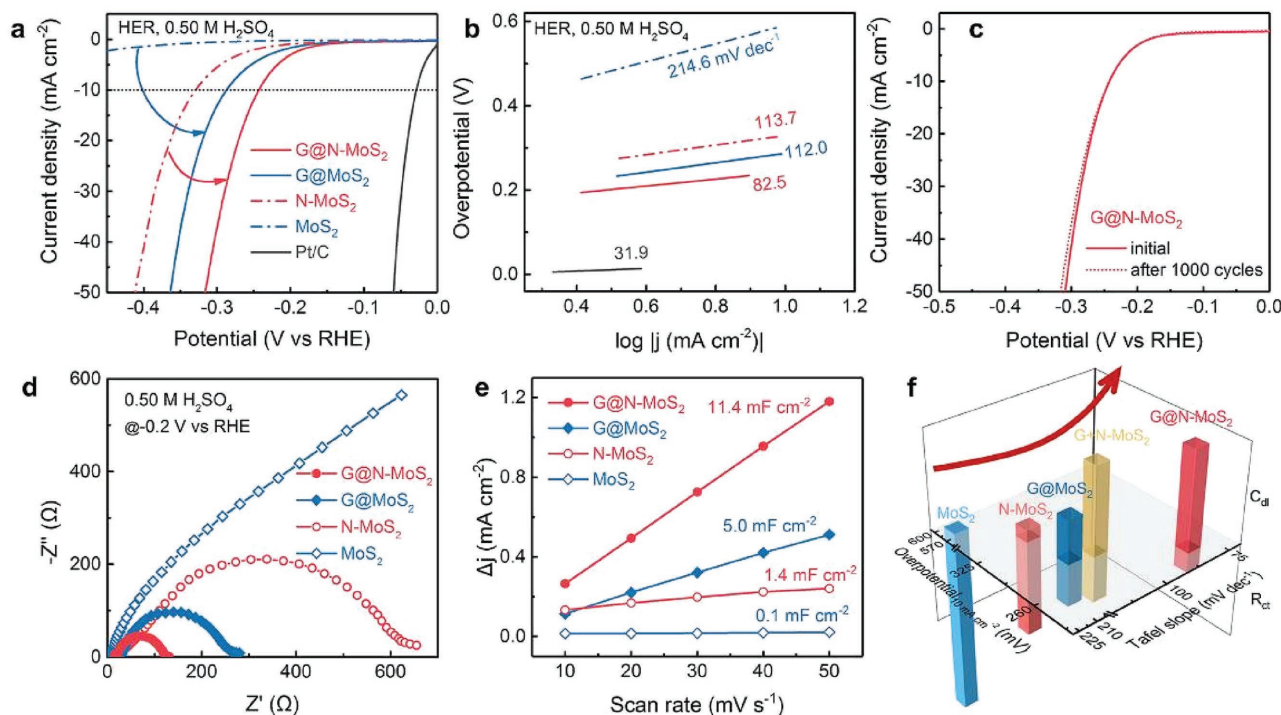
Figure 4. Electrocatalytic HER performance of 3D mesoporous G@N-MoS$_2$ heterostructures. a) HER polarization curves for different electrocatalysts. b) Tafel plots corresponding to the tests in panel (a). c) Polarization curves recorded for G@N-MoS$_2$ before and after 1000 cycles of CV scan. d) EIS Nyquist plots collected under overpotential of 200 mV. e) Calculated C_{dl} for different samples, equivalent to the half of the slope. f) The correlation between activity (Tafel slope and overpotential for 10 mA cm^{-2}) and property (double-layer capacitance and charge transfer resistance). All measurements were conducted in N$_2$-saturated 0.50 M H$_2$SO$_4$ solution at 25 °C, with a catalyst loading of ≈0.25 mg cm^{-2}.

**ADVANCED
SCIENCE NEWS**

www.advancedsciencenews.com

**ADVANCED
MATERIALS**

www.advmat.de

is nearly decreased to one-tenth of that for MoS_2 (Figure 4d), which suggests a significantly improved electron transfer and thus a good HER activity as shown in Figure 4a. In addition, the nitrogen doping is revealed to be able to further reduce the R_{ct} and improve the electrocatalytic activity.[23] Furthermore, the double-layer capacitance (C_{dl}) values of as-obtained vdW heterostructures are one or two orders of magnitude larger than their counterparts without graphene, and can be substantially increased by the nitrogen doping in MoS_2 (Figure 4e). On one hand, the 3D mesoporous graphene framework not only compensates the poor electrical conductivity of 2H MoS_2 phase and facilitates the mass transport for a higher accessibility of active sites, but also manipulates the morphology of the subsequent N-MoS_2 nanosheets with fully exposed active edges and strain-derived active sites.[25,30] On the other hand, the N dopants in MoS_2 can decrease the bandgap and spread conducting charges over the basal plane, thus further increasing the conductivity and facilitating charge transfer.[23] The substitution of S by N atoms is demonstrated to induce p-type doping of MoS_2 with compressive strains[31] and sulfur vacancies,[23] which can activate the S atoms at edge[23] or adjacent to N dopants[22] and benefit the Mo edges as well.[23]

Consequently, the G@N-MoS_2 yields the lowest R_{ct} (99 Ω) and highest C_{dl} (11.4 mF cm^{-2}) values attributed to the synergistic effect of graphene hybridization and nitrogen doping, thereby resulting in the best HER activity. To advance the elucidation, the properties and activities of the physical mixture of G and N-MoS_2 samples (G+N-MoS_2) were further investigated. Despite a large C_{dl} (10.1 mF cm^{-2}) approaching that for G@N-MoS_2 (Figure S12, Supporting Information), the calculated R_{ct} value for G+N-MoS_2 is more than twice and even larger than that for G@MoS_2 (Figure S13, Supporting Information). Accordingly, the HER activity of G+N-MoS_2 is just comparable with G@MoS_2, but considerably inferior to G@N-MoS_2, with the η_{10} increased by 40 mV (Figure S14, Supporting Information). It can be rationalized by the strongly coupled interfaces in addition to the individual graphene hybridization and nitrogen doping in such vertical vdW heterostructure, which will be discussed below. Figure 4f visualizes the relationship between properties (C_{dl} and R_{ct}) and activities (η_{10} and Tafel slope) for all samples, vividly revealing that the 3D mesoporous G@N-MoS_2 vdW heterostructure can effectively provide an all-round engineering of 2D materials toward optimized electrocatalytic performance.

Encouraged by the significantly improved electrocatalytic activities for HER in acid, we continued to evaluate the activity of 3D mesoporous G@N-MoS_2 vdW heterostructures for HER, ORR, and OER in alkaline. The efficient catalysis for HER coupled with OER is of paramount importance to the clean hydrogen production by electrochemical water splitting; meanwhile, the ORR and OER electrocatalysis is crucial for some renewable energy technologies, such as fuel cells and metal–air batteries.[32,33] In contrast to the tremendous research of MoS_2 for HER, there are only few reports considering their applications for ORR[34–36] or OER.[5,37] The abundant Mo edge sites in MoS_2 nanoparticles[5,34,37] and the spin densities altered by heteroatom doping (such as N and P)[35,36] are revealed to be responsible for the ORR/OER activity of MoS_2-based electrocatalysts. Most recently, the topological defects in porous graphene

are also believed to be a kind of effective active centers toward ORR, OER, and HER.[33,38] Therefore, G@N-MoS_2 is expected to provide abundant active sites for multifunctional electrocatalysis attributed to the unique structure and properties as discussed in the case of HER.

As shown in **Figure 5**a–c, G@N-MoS_2 exhibits the best trifunctional electrocatalytic activities for ORR/OER/HER in 0.10 M KOH among all samples. In the HER experiment, the onset potential for G@N-MoS_2 is positively shifted by more than 100 mV compared with other counterparts (Figure 5a) and even better than that in acid (Figure 4a). The difference of η_{10} between G@N-MoS_2 and Pt/C is shown to be prominently reduced by 60 mV, further indicating the remarkable HER activity in alkaline. Besides, the ORR limiting current density for G@N-MoS_2 approaches that of Pt/C, and the half-wave potential difference between them is 83 mV, much smaller than those for G (110 mV), N-MoS_2 (495 mV), and G@MoS_2 (177 mV) (Figure 5b). Moreover, the OER activity of G@N-MoS_2 is revealed to be competitive with the precious Ir/C catalyst, even with a lower η_{10} decreased by 20 mV (Figure 5c). The potential gap (ΔE) between the potential required for a current density of 10 mA cm^{-2} for OER and half-wave potential for ORR is determined to be ≈0.90 V for G@N-MoS_2 and superior to the precious metal-based catalysts (e.g., Ir/C: ≈1.05 V), implying the promising multifunctional electrocatalytic activities (Table S2, Supporting Information).

It should be pointed out, however, the ORR activities for G@MoS_2 and G+N-MoS_2 are demonstrated to be inferior to the pristine G sample, with more negative onset potential and higher overpotential (Figure S15, Supporting Information). The OER activity of G+N-MoS_2 is also significantly poorer than G with much higher overpotential (Figure S16, Supporting Information). These unexpected results strongly indicate that the (N-)MoS_2 may not exhibit good activities for ORR and OER, which is at least inferior to the mesoporous graphene framework. Inevitably, the high ORR/OER activity of G@N-MoS_2 should be attributed to some particular strengthening effects originated from the novel 3D mesoporous vdW heterostructure.

It has been reported that in the G/MoS_2 vertical heterostructure, electrons will transfer from MoS_2 to graphene due to their different work functions as illustrated in Figure 5d.[18] The electron transfer can form a built-in electric field and induce excessive negative charge density on MoS_2,[18] and decrease the bandgap at MoS_2 edges[12] to enhance the corresponding electrocatalysis. Moreover, the nitrogen doping can effectively modulate the electronic properties of MoS_2 with higher spin densities[35] and decreased bandgap,[23] which is expected to further strengthen the interfacial charge transfer. Therefore, in addition to the graphene hybridization and nitrogen doping, the strongly coupled interface in G@N-MoS_2 can effectively induce the charge redistribution and modify the electronic properties, leading to optimized adsorption energies. Consequently, the electrocatalytic activity of each component is expected to be improved, and thereby enabling promising trifunctional electrocatalysis.[14] Based on the above discussion, the enhanced HER is supposed to conduct on N-MoS_2, while the ORR and OER activities are improved on graphene (Figure 5d). The clear mechanism of the trifunctional activity enhancement in such

ADVANCED
SCIENCE NEWS
www.advancedsciencenews.com

ADVANCED
MATERIALS
www.advmat.de
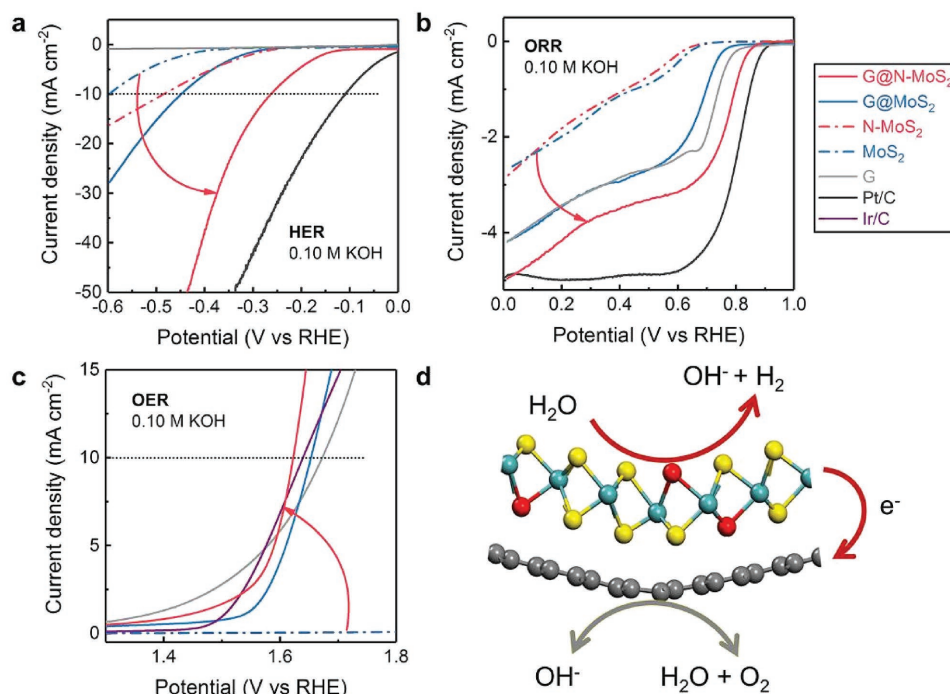
Figure 5. Trifunctional energy electrocatalytic activity of 3D mesoporous G@N-MoS$_2$ heterostructures. a) HER polarization curves obtained in N$_2$-saturated 0.10 M KOH solution. b) ORR and c) OER polarization curves obtained in O$_2$-saturated 0.10 M KOH solution. d) Schematic representation of the electron transfer effects in G@N-MoS$_2$ heterostructures toward improved electrocatalytic activities for ORR, OER, and HER.

3D mesoporous vdW heterostructure still requires investigation by first-principles calculations.

In summary, we have constructed a 3D mesoporous vdW heterostructure of graphene and N-MoS$_2$ via a two-step sequential CVD method. Ultrathin N-MoS$_2$ nanosheets are locally curved and intimately merged with the previously deposited graphene to form a vertical vdW heterostructure and 3D mesoporous framework, which is demonstrated to afford multifunctional modifications of 2D materials: (1) morphology engineering: the 3D mesoporous structure facilitates mass transport of reactants and accessibility of active sites; (2) edge engineering: the nanosized and ultrathin N-MoS$_2$ exposes more active edge sites; (3) defect engineering: the topological curvature and nitrogen doping induce abundant strains and defects with new active centers; (4) interface engineering: the interfacial charge redistribution in the vdW heterostructure facilitates the electron transfer and modifies the adsorption energies of intermediates; (5) electronic engineering: the strong coupling with graphene and nitrogen doping enhance the electrical conductivity and electrocatalytic activity of 2H N-MoS$_2$ basal planes. Consequently, remarkably enhanced electrocatalytic activities are achieved attributed to the 3D vdW heterostructure and N doping, with accelerated HER on MoS$_2$ and improved ORR/OER on graphene. The performance is believed to be further promoted by the optimization of each components and the 3D nanostructure. This work provides fresh concepts for the development of advanced nanomaterials and paves new ways to comprehensively engineer and optimize the properties of various 2D materials, aiming at highly effective energy electrocatalysis and other applications.

Experimental Section

Materials Synthesis: The mesoporous MgO template was prepared by surfactant-assisted hydrothermal reaction. Typically, 2.12 g polyethylene glycol-2000 was dispersed in 200 mL deionized water, then 1.0 g commercial MgO powders (99.5%) were added slowly under continuous stirring and the whole mixture was further stirred overnight, followed by the hydrothermal reaction at 180 °C for 48.0 h in a 250 mL Teflon-lined stainless steel autoclave. The MgO templates were obtained after the product was filtered, washed, freeze dried, and calcined at 650 °C for 5.0 h under air.

The 3D mesoporous G@N-MoS$_2$ heterostructure was synthesized by two-step sequential CVD growth in a double temperature-zone furnace. First, sulfur (≈300 mg, 99.999%), MoCl$_5$ (≈150 mg, 99.99%), and as-obtained MgO powders (≈500 mg) were sprayed in separate ceramic boats, which were placed at the entry of first-zone, the center of first-zone, and the center of second-zone. Then, the second-zone was heated to 950 °C without heating the first-zone under flowing Ar (≈100 mL min^{-1}), followed by the introduction of CH$_4$ (≈70 mL min^{-1}) for 5.0 min to deposit graphene. After that, the second-zone was cooled to 800 °C, while the first-zone was heated up. When the temperature reached 400 °C, NH$_3$ (≈50 mL min^{-1}) was introduced into the reactor. Then the first-zone was continuously heated to 800 °C and maintained for 30 min for the deposition of N-MoS$_2$. The final product was purified by hydrochloric acid (1.0 mol L^{-1}) at 80 °C for 24.0 h to remove the MgO templates. After washing, filtering, and freeze-drying, G@N-MoS$_2$ was obtained.

G@MoS$_2$ was prepared under otherwise identical conditions without NH$_3$ introduction. G was prepared without the subsequent deposition of N-MoS$_2$, while N-MoS$_2$ was prepared without the previous growth of graphene. G+N-MoS$_2$ was prepared simply by mixing N-MoS$_2$ and G.

Characterization: The morphology and structure of the samples were characterized using a JSM 7401F (JEOL Ltd., Tokyo, Japan) SEM operated at 3.0 kV and a JEM 2010 (JEOL Ltd., Tokyo, Japan) TEM operated at 120.0 kV. HAADF-STEM was collected on an FEI Tecnai G2

F20TEM. The EELS data were recorded on an FEI Tecnai G 2 F20 TEM equipped with Gatan Image Filter. XRD patterns were recorded on a Bruker D8 Advance diffractometer at 40.0 kV and 120 mA with Cu Kα radiation. XPS tests were carried out by ESCALAB 250xi. The N_2 adsorption–desorption isotherm was collected using an Autosorb-IQ2-MP-C system. The specific surface area was calculated by the multipoint Brunauer–Emmett–Teller method. Raman spectra were obtained using a Horiba Jobin Yvon LabRAM HR800 Raman spectrophotometer.

Electrocatalytic Performance Measurements: Electrochemical measurements were performed on a rotating disk electrode (RDE) (Pine Research Instrument, USA) in a three-electrode electrochemical setup using a computer-controlled electrochemistry workstation (CHI 760D, CH Instrument, USA). A graphite rod electrode and a saturated calomel electrode (SCE) served as the counter and reference electrodes, respectively.

The working electrode was fabricated by the drop casting method. 5.0 mg of specific catalysts was first dispersed in 0.95 mL ethanol and 0.05 mL Nafion solution (5.0 wt%), followed by 1.0 h sonication to form a relatively homogeneous suspension. Then 10.0 µL of the suspension was pipetted onto the glass carbon (GC) electrode (0.196 cm^2) via a controlled drop casting approach. After solvent evaporation for 10.0 min in air, the catalyst clung to the GC electrode to serve as the working electrode.

The HER activity was tested both in N_2-saturated 0.50 M H_2SO_4 solution and N_2-saturated 0.10 M KOH solution, and OER/ORR activities were tested in O_2-saturated 0.10 M KOH. The RDE rotated at 1600 rpm for all tests. The working electrodes were cycled several times by CV before other measurements. LSV curves were tested at a scan rate of 10.0 mV s^{-1} with 95% iR-compensation. The potential (E) versus reversible hydrogen electrode (RHE) was calculated by the following equation: E versus RHE = E versus SCE (measured value) + 0.0592 pH + 0.241.

The HER durability in N_2-saturated 0.50 M H_2SO_4 solution was tested by LSV after 1000 cycles of CV (0 to −0.25 V vs RHE). The ECSA was determined by measuring the capacitive current associated with double-layer charging from the scan-rate dependence of CV. This measurement was performed on the same working electrode in a potential window of 0.02–0.10 V versus RHE with scan rates ranging from 10 to 50 mV s^{-1}. Then linear fitting of the charging current density differences ($\Delta j = j_a - j_c$ at a potential of 0.06 V vs RHE) against the scan rate was done. The slope is twice the C_{dl}, which is used to represent ECSA. The EIS test was carried out on the working electrodes at a potential of −0.20 V versus RHE. The spectra were collected in a frequency range of 10^{-2}–10^6 Hz with an amplitude of 5.0 mV.

Supporting Information

Supporting Information is available from the Wiley Online Library or from the author.

Acknowledgements

Conflict of Interest

The authors declare no conflict of interest.

[1] K. S. Novoselov, A. K. Geim, S. V. Morozov, D. Jiang, Y. Zhang, S. V. Dubonos, I. V. Grigorieva, A. A. Firsov, *Science* **2004**, *306*, 666.

[2] a) Y. Zheng, Y. Jiao, Y. H. Zhu, L. H. Li, Y. Han, Y. Chen, A. J. Du, M. Jaroniec, S. Z. Qiao, *Nat. Commun.* **2014**, *5*, 3783; b) D. Voiry, J. Yang, M. Chhowalla, *Adv. Mater.* **2016**, *28*, 6197; c) Q. Ding, B. Song, P. Xu, S. Jin, *Chem* **2016**, *1*, 699.

[3] a) L. Qu, Y. Liu, J.-B. Baek, L. Dai, *ACS Nano* **2010**, *4*, 1321; b) X. Liu, L. Dai, *Nat. Rev. Mater.* **2016**, *1*, 16064.

[4] a) F. Song, X. Hu, *Nat. Commun.* **2014**, *5*, 4477; b) S. Chen, J. Duan, M. Jaroniec, S.-Z. Qiao, *Adv. Mater.* **2014**, *26*, 2925; c) B. Q. Li, C. Tang, H. F. Wang, X. L. Zhu, Q. Zhang, *Sci. Adv.* **2016**, *2*, e1600495; d) X. Zhang, X. Cheng, Q. Zhang, *J. Energy Chem.* **2016**, *25*, 967.

[5] J. J. Wu, M. J. Liu, K. Chatterjee, K. P. Hackenberg, J. F. Shen, X. L. Zou, Y. Yan, J. Gu, Y. C. Yang, J. Lou, P. M. Ajayan, *Adv. Mater. Interfaces* **2016**, *3*, 1500669.

[6] a) P. F. Yang, Z. P. Zhang, J. P. Shi, S. L. Jiang, Y. F. Zhang, *ChemNanoMat* **2017**, *3*, 340; b) Z. Zhang, P. Chen, X. Duan, K. Zang, J. Luo, X. Duan, *Science* **2017**, *357*, 788.

[7] R. K. Biroju, D. Das, R. Sharma, S. Pal, L. P. L. Mawlong, K. Bhorkar, P. K. Giri, A. K. Singh, T. N. Narayanan, *ACS Energy Lett.* **2017**, *2*, 1355.

[8] A. K. Geim, I. V. Grigorieva, *Nature* **2013**, *499*, 419.

[9] Y. Lei, S. Pakhira, K. Fujisawa, X. Y. Wang, O. O. Iyiola, N. P. Lopez, A. L. Elias, L. P. Rajukumar, C. J. Zhou, B. Kabius, N. Alem, M. Endo, R. T. Lv, J. L. Mendoza-Cortes, M. Terrones, *ACS Nano* **2017**, *11*, 5103.

[10] K. S. Novoselov, A. Mishchenko, A. Carvalho, A. H. Castro Neto, *Science* **2016**, *353*, aac9439.

[11] X. L. Zheng, J. B. Xu, K. Y. Yan, H. Wang, Z. L. Wang, S. H. Yang, *Chem. Mater.* **2014**, *26*, 2344.

[12] J. P. Shi, X. B. Zhou, G. F. Han, M. X. Liu, D. L. Ma, J. Y. Sun, C. Li, Q. Q. Ji, Y. Zhang, X. J. Song, X. Y. Lang, Q. Jiang, Z. F. Liu, Y. F. Zhang, *Adv. Mater. Interfaces* **2016**, *3*, 1600332.

[13] J. Duan, S. Chen, B. A. Chambers, G. G. Andersson, S. Z. Qiao, *Adv. Mater.* **2015**, *27*, 4234.

[14] Y. Jia, L. Z. Zhang, G. P. Gao, H. Chen, B. Wang, J. Z. Zhou, M. T. Soo, M. Hong, X. C. Yan, G. R. Qian, J. Zou, A. J. Du, X. D. Yao, *Adv. Mater.* **2017**, *29*, 1700017.

[15] a) X. Long, J. Li, S. Xiao, K. Yan, Z. Wang, H. Chen, S. Yang, *Angew. Chem., Int. Ed.* **2014**, *53*, 7584; b) C. Tang, H. F. Wang, X. L. Zhu, B. Q. Li, Q. Zhang, *Part. Part. Syst. Charact.* **2016**, *33*, 473; c) W. Ma, R. Ma, C. Wang, J. Liang, X. Liu, K. Zhou, T. Sasaki, *ACS Nano* **2015**, *9*, 1977.

[16] T. Y. Ma, J. L. Cao, M. Jaroniec, S. Z. Qiao, *Angew. Chem., Int. Ed.* **2015**, *55*, 1138.

[17] Y. Jiao, Y. Zheng, K. Davey, S. Z. Qiao, *Nat. Energy* **2016**, *1*, 16130.

[18] H. L. Li, K. Yu, C. Li, Z. Tang, B. J. Guo, X. Lei, H. Fu, Z. Q. Zhu, *Sci. Rep.* **2015**, *5*, 18730.

[19] C. Tang, H. S. Wang, H. F. Wang, Q. Zhang, G. L. Tian, J. Q. Nie, F. Wei, *Adv. Mater.* **2015**, *27*, 4516.

[20] Y. F. Yu, C. Li, Y. Liu, L. Q. Su, Y. Zhang, L. Y. Cao, *Sci. Rep.* **2013**, *3*, 1866.

ADVANCED
SCIENCE NEWS
www.advancedsciencenews.com

ADVANCED
MATERIALS
www.advmat.de

[21] a) P. T. Liu, J. Y. Zhu, J. Y. Zhang, P. X. Xi, K. Tao, D. Q. Gao, D. S. Xue, *ACS Energy Lett.* **2017**, *2*, 745; b) Z. F. Ye, J. Yang, B. Li, L. Shi, H. X. Ji, L. Song, H. X. Xu, *Small* **2017**, *13*, 1700111.

[22] R. C. Li, L. J. Yang, T. L. Xiong, Y. S. Wu, L. D. Cao, D. S. Yuan, W. J. Zhou, *J. Power Sources* **2017**, *356*, 133.

[23] W. Xiao, P. T. Liu, J. Y. Zhang, W. D. Song, Y. P. Feng, D. Q. Gao, J. Ding, *Adv. Energy Mater.* **2017**, *7*, 1602086.

[24] H. Li, Q. Zhang, C. C. R. Yap, B. K. Tay, T. H. T. Edwin, A. Olivier, D. Baillargeat, *Adv. Funct. Mater.* **2012**, *22*, 1385.

[25] Y. W. Tan, P. Liu, L. Y. Chen, W. T. Cong, Y. Ito, J. H. Han, X. W. Guo, Z. Tang, T. Fujita, A. Hirata, M. W. Chen, *Adv. Mater.* **2014**, *26*, 8023.

[26] a) Q. H. Liu, W. J. Xia, Z. J. Wu, J. Huo, D. D. Liu, Q. Wang, S. Y. Wang, *Nanotechnology* **2016**, *27*, 175402; b) S. Qin, W. W. Lei, D. Liu, Y. Chen, *Sci. Rep.* **2014**, *4*, 7582.

[27] a) Y. Yang, H. L. Fei, G. D. Ruan, C. S. Xiang, J. M. Tour, *Adv. Mater.* **2014**, *26*, 8163; b) G. R. Bhimanapati, T. Hankins, Y. Lei, R. A. Vila, I. Fuller, M. Terrones, J. A. Robinson, *ACS Appl. Mater. Interfaces* **2016**, *8*, 22190.

[28] D. H. Youn, S. Han, J. Y. Kim, J. Y. Kim, H. Park, S. H. Choi, J. S. Lee, *ACS Nano* **2014**, *8*, 5164.

[29] C. Tsai, F. Abild-Pedersen, J. K. Norskov, *Nano Lett.* **2014**, *14*, 1381.

[30] J. Deng, H. B. Li, S. H. Wang, D. Ding, M. S. Chen, C. Liu, Z. Q. Tian, K. S. Novoselov, C. Ma, D. H. Deng, X. H. Bao, *Nat. Commun.* **2017**, *8*, 14430.

[31] A. Azcatl, X. Y. Qin, A. Prakash, C. X. Zhang, L. X. Cheng, Q. X. Wang, N. Lu, M. J. Kim, J. Kim, K. Cho, R. Addou, C. L. Hinkle, J. Appenzeller, R. M. Wallace, *Nano Lett.* **2016**, *16*, 5437.

[32] a) C. G. Hu, L. M. Dai, *Adv. Mater.* **2017**, *29*, 1604942; b) J. T. Zhang, L. M. Dai, *Angew. Chem., Int. Ed.* **2016**, *55*, 13296.

[33] Y. Jia, L. Z. Zhang, A. J. Du, G. P. Gao, J. Chen, X. C. Yan, C. L. Brown, X. D. Yao, *Adv. Mater.* **2016**, *28*, 9532.

[34] T. Y. Wang, D. L. Gao, J. Q. Zhuo, Z. W. Zhu, P. Papakonstantinou, Y. Li, M. X. Li, *Chem.- Eur. J.* **2013**, *19*, 11939.

[35] H. Y. Zhang, Y. Tian, J. X. Zhao, Q. H. Cai, Z. F. Chen, *Electrochim. Acta* **2017**, *225*, 543.

[36] H. Huang, X. Feng, C. C. Du, S. Y. Wu, W. B. Song, *J. Mater. Chem. A* **2015**, *3*, 16050.

[37] K. Yan, Y. R. Lu, *Small* **2016**, *12*, 2975.

[38] a) C. Tang, H.-F. Wang, X. Chen, B.-Q. Li, T.-Z. Hou, B. Zhang, Q. Zhang, M.-M. Titirici, F. Wei, *Adv. Mater.* **2016**, *28*, 6845; b) C. Tang, Q. Zhang, *Adv. Mater.* **2017**, *29*, 1604103; c) D. Yan, Y. Li, J. Huo, R. Chen, L. Dai, S. Wang, *Adv. Mater.* **2017**, *29*, 1606459; d) Z. J. Liu, Z. H. Zhao, Y. Y. Wang, S. Dou, D. F. Yan, D. D. Liu, Z. H. Xia, S. Y. Wang, *Adv. Mater.* **2017**, *29*, 1606207.

1705110 (8 of 8)